Corrosion Science 83 (2014) 409–418

Contents lists available at ScienceDirect

Corrosion Science

journal homepage: www.elsevier.com/locate/corsci

In situ 3D monitoring of corrosion on carbon steel and ferritic stainless steel embedded in cement paste

Pierre-Adrien Itty [a,*], Marijana Serdar [a,c], Cagla Meral [a,d], Dula Parkinson [b], Alastair A. MacDowell [b], Dubravka Bjegović [c], Paulo J.M. Monteiro [a]

[a] Department of Civil and Environmental Engineering, University of California, Berkeley, CA 94720, United States
[b] Lawrence Berkeley National Laboratory, 1 Cyclotron Road, Berkeley, CA 94720, United States
[c] Department of Materials, Faculty of Civil Engineering, University of Zagreb, 10000 Zagreb, Croatia
[d] Department of Civil Engineering, Middle East Technical University, 06800 Ankara, Turkey

ARTICLE INFO

Article history:
Received 10 October 2013
Accepted 3 March 2014
Available online 11 March 2014

Keywords:
A. Steel reinforced concrete
A. Stainless steel
B. Galvanostatic
C. Interfaces
C. Pitting corrosion

ABSTRACT

In a X-ray microcomputed tomography study, active corrosion was induced by galvanostatically corroding steel embedded in cement paste. The results give insight into corrosion product build up, crack formation, leaching of products into the cracks and voids, and differences in morphology of corrosion attack in the case of carbon steel or stainless steel reinforcement. Carbon steel was homogeneously etched away with a homogeneous layer of corrosion products forming at the steel/cement paste interface. For ferritic stainless steel, pits were forming, concentrating the corrosion products locally, which led to more extensive damage on the cement paste cover.

© 2014 Elsevier Ltd. All rights reserved.

1. Introduction

The corrosion process of the reinforcing steel in concrete can be divided into two time periods: the initiation period and the propagation period [1]. During the initiation period the conditions for passive film break down and initiation of corrosion develop. During the propagation period, iron reacts with oxygen and water to form corrosion products, mainly iron oxide/hydroxides. Because the latter have larger specific volumes than metallic iron [2], corrosion products begin to inhabit the steel/concrete porous interfacial zone, generating radial pressure [3–5], and consequently causing cracking of concrete. Since predicting the time to concrete cracking could lead to significant decrease in repair costs and safety during structures' operation, numerous service life models are developed in order to monitor and predict the time to cracking due to the corrosion of reinforcement [3,4,6,7].

Predicting the stability and serviceability of structures requires crucial information about the propagation period, such as at what point do corrosion products begin accumulating at the steel/concrete interface, eventually leading to corrosion-induced cracking of the surrounding concrete. Although several models have been developed that predict the time-to-corrosion cracking, taking into account the nonlinear formation of corrosion products [4], and the residual mechanical properties of concrete and reinforcement during corrosion [3,8], differences between model predictions and experimental results remain. These difference are attributed to two factors: (1) a lack of understanding of the composition, mechanical properties, and transport of the corrosion products filling the porous zone and surrounding voids and pores [5,8,9]; and (2) most models assume a uniform layer of corrosion products around the steel/concrete interface, which is not accurate enough for characterizing the chloride-induced corrosion of steel reinforcement, as highlighted in the work by Zhao et al. [10].

The difference between uniform and localized corrosion becomes more pronounced in the case of stainless steel. With increasing demand of prolonging the service life of structures in aggressive environments, researchers have considered replacing carbon steel with stainless steels with lower concentrations of chromium and nickel [11–13]. These grades of steel can be used where the high cost/high corrosion resistance of austenitic stainless steel is not required e.g., for structures subjected to mild marine environments [14]. For stainless steel, the attack can be extremely localized with the formation of corrosion pits [15–18]. During localised corrosion a local loss of steel cross section takes place, which can induce dramatic consequences for reinforced and prestressed concrete structures under load. In addition, with

* Corresponding author. Address: Schlumberger Riboud Product Center, 1 rue Henri Becquerel, 92140 Clamart, France.
E-mail address: pitty@slb.com (P.-A. Itty).

http://dx.doi.org/10.1016/j.corsci.2014.03.010
0010-938X/© 2014 Elsevier Ltd. All rights reserved.

the pressure from the corrosion products forming locally, it could lead to local increase of stresses at the steel/concrete interface.

Until now the formation of pits has been limited to investigations of stainless steel alone [15,18–20], but the kinetics of formation of these pits inside cement paste deserves increased attention. Most of the time, mechanisms of corrosion propagation were inferred from indirect observation methods: (1) a "destructive" approach, which requires cutting open the samples after evidence of extensive corrosion [21]; or (2) external observations of apparent crack propagation [5,6]. These indirect methods give valuable insight into the extent of corrosion; however, information about the corrosion products themselves is limited. When observing an open sample, cracks might have been induced in preparation of the sample, corrosion products may have been displaced, and additional oxidation, as a result of the preparation environment, might change their nature. Furthermore, information about morphology and volume of the studied phases is lost through visual observation [22]. Recently, initiatives for investigating the propagation period of reinforcement in concrete by non-destructive methods have been developed, such as X-ray attenuation measurement [23]; however, this work was limited by the low resolution of the X-ray camera—pixel size was 0.89 mm × 0.89 mm—and the lack of full three-dimensional (3D) information on the 2-cm-thick mortar samples.

The work presented herein demonstrates the unique advantages of X-ray microcomputed tomography (μCT) using synchrotron radiation to follow corrosion formation in cement paste. The technique allows for real time *in situ* 3D characterization of the following mechanisms: (1) corrosion of the steel reinforcement; (2) accumulation of corrosion products at the steel/concrete interface; and (3) development of cracks in the cement paste matrix. The main advantages of using μCT is that it is non-invasive, enables real-time monitoring without interfering with the chemistry and the morphology of the products and cracks, and offers the possibility of 3D-imaging of the morphology of the structure. Because the technique is sensitive to the density of materials, the different phases – steel, corrosion products, and cement matrix – are distinguishable. A similar μCT technique has already been successfully used to study concrete [24], steel corrosion [16,18,25,26], voids and defects in materials [27–29]. Monteiro et al. also highlighted the efficacy of μCT in quantifying issues concerned with the durability of concrete [30].

The aim of the experimental work was to use μCT technique for comparison of behaviour of carbon and ferritic stainless steels embedded in cement paste and exposed to accelerated corrosion by imposing high current density. Samples were galvanostatically corroded for 3 h with a constant anodic current of 5 mA cm^{-2} and were periodically analysed using μCT. The obtained 3D datasets, along with the polarisation curve, determined the mechanism of galvanostatic corrosion of steel inside concrete. A binary segmentation of the steel reinforcement helped to understand the kinetic of the corrosion pitting by computing its average and maximum penetrations, and comparing it with the penetration computed by the mass loss equation. Finally a detailed description of the corrosion product accumulation at the steel/cement paste interface and their further propagation through the corrosion-induced crack network was obtained. It shall be noted that corrosion process occurring due to the impressed current is very different from that occurring naturally by chloride-induced corrosion, as highlighted in details in the work by Poursaee and Hansson in [31]. Accelerating corrosion with impressed current can modify the corrosion mechanism, change the chemical conditions around reinforcing steel, alter the type of corrosion products formed, and induce high strain responses and crack widths [31–33]. Therefore, results presented in this paper and resulting conclusions should be limited to the comparison of corrosion behaviour of two grades of steel in cement paste under the same conditions of accelerated corrosion.

2. Materials and methods

2.1. Materials

The steel samples under investigation were composed of two different steels: carbon steel (ASTM A36), labelled CS, and low-nickel ferritic stainless steel (UNS S41000), labelled FSS. See Table 1 for a list of their elemental compositions.

Three samples for each combination of steel were prepared, 6 samples in total. #10 reinforcing bars were cut, thinned, and polished to create cylinders that were approximately 0.5 mm in diameter, and 5 mm in length. Isolated electrical wires were then connected to them to ensure the electrical connection. This connection between the steel and the wire was covered with impermeable paint to minimize the risk of corrosion of the wire and galvanic corrosion between the two (Fig. 1). The carbon steel specimen was 0.46 mm in diameter and had an exposed length of 3.5 mm; the ferritic stainless steel was 0.37 mm in diameter and had an exposed length of 3.6 mm. The specimens were placed into cylindrical moulds, 5 mm in diameter, and cement paste was poured into them. The cement paste was produced by mixing water with ordinary Portland cement type II at a water-to-cement ratio of 0.40. Once cement paste was poured in the mould, samples were placed for one day in humidity chamber (95% RH), to ensure sufficient humidity and minimize risk of shrinkage and consequent cracking. Next, the specimens were demoulded and subjected to additional curing in humidity chamber for 90 days.

It is important to highlight that the total size of samples was constrained by two things: the diameter of reinforcing rebar needed to be smaller than 0.5 mm in order to achieve optimal X-ray transmission through steel, and the thickness of concrete cover needed to be higher than 2 mm, in order to permit the pouring of the cement paste. For the purpose of this research numerous samples were prepared, and only not cracked samples, without gaps and pockets around reinforcement were used for further investigation.

2.2. Electrochemical cell

To conduct the electrochemical measurements, a three-electrode cell was used with the described reinforced cement paste sample used as working electrode, a Saturated Calomel Electrode (SCE) as reference electrode, and a stainless steel mesh surrounding the sample as counter electrode (Fig. 2). The samples were placed in a solution containing 3.5% per mass of sodium chloride to support the electron transfer. The end of the electrical wires was then electrically connected to a GAMRY PCI4/750 potentiostat/galvanostat. All potentials were measured with respect to the Saturated Calomel Electrode (SCE). The solution was considered saturated with respect to oxygen. Galvanostatic corrosion of the steel reinforcement was performed by imposing a constant anodic current density, i_G, of 5 mA cm^{-2} for similar lengths of time for the separate samples. The potential of the steels during galvanostatic corrosion, E_G, was measured with respect to the reference electrode to evaluate its corrosion evolution. The samples were taken out of solution at three different times, when a sudden decrease of potential was evident, and left at the open circuit potential during μCT imaging.

2.3. Micro X-ray computed tomography (μCT)

μCT experiments were conducted at beamline 8.3.2 of the Advanced Light Source at the Lawrence Berkeley National Laboratory [34]. The principle of X-ray tomography technique is to detect the intensity of the transmitted fraction of X-rays passing through the

Table 1
Chemical composition of carbon steel (CS) and ferritic stainless steel (FSS).

	Chemical composition, wt.%										
	C	Si	Mn	P	S	N	Cr	Cu	Mo	Ni	Fe
CS	0.19	0.10	0.62	0.020	0.022	0.005	0.07	0.04	<0.02	0.02	Bal.
FSS	0.018	0.80	0.56	0.013	<0.001	0.01	12.37	0.02	0.02	0.46	Bal.

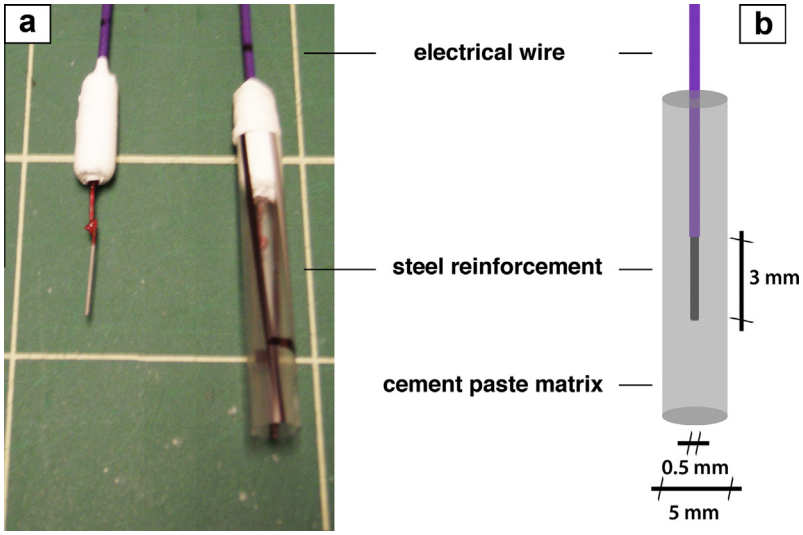


Fig. 1. (a) Thinned reinforcing bar soldered to the electrical wire, reinforcing bar, and wire centred in the mould; and (b) schematic with the average dimensions of the sample for micro-computed tomography.

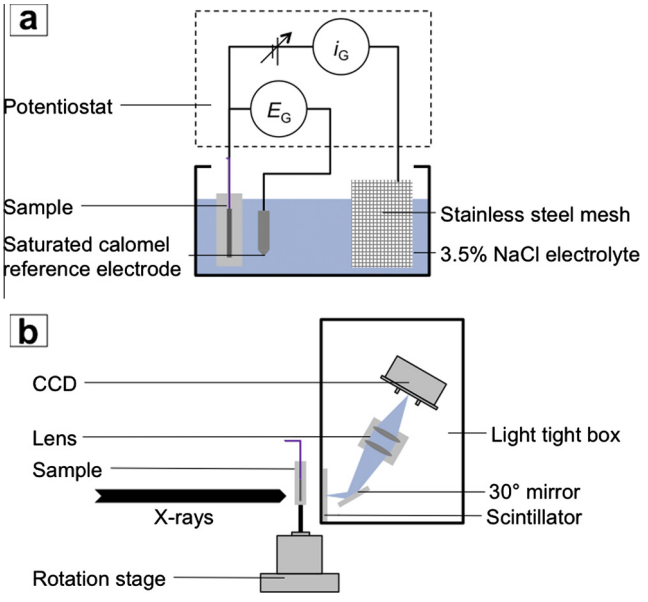


Fig. 2. (a) Electrochemical setup used for galvanostatic corrosion showing the potentiostat and the three-electrode cell; and (b) the X-ray micro-computed tomography setup.

sample (Fig. 2). When single photon energy beam is used in absorption mode, the intensity, I, of the X-ray beam leaving a multi-component system, and detected on the detector is attenuated following Beer's law:

$$I = I_0 \exp\left(-\sum \mu_i t_i\right) \quad (1)$$

where I_0 is the initial intensity, μ_i is the linear attenuation coefficient of component i, and t_i is the thickness of component i. The linear attenuation coefficient is specific for different materials and depends on the energy of the beam. Therefore, during testing for each pixel (x', z) on the detector the attenuated value, P, is then determined by:

$$P(x', z) = -\ln\left(\frac{I(x', z)}{I_0}\right) \quad (2)$$

During a scan, the sample is mounted on the rotation stage, allowing for X-ray transmission images to be captured at various rotation angles, φ. The attenuated value on the detector is hence the Radon transform of the linear attenuation field, $\mu(x, y, z)$:

$$P(\varphi, x', z) = \iint_{\Omega} \mu(x, y, z)\delta(x\cos\varphi + y\sin\varphi - x')\mathrm{d}x\mathrm{d}y \quad (3)$$

The linear attenuation field, $\mu(x, y, z)$, gives a 3D representation of the sample. Using the Fourier slice theorem, $\mu(x, y, z)$ is obtained for all x, y, and z by inverting the expression for $P(\varphi, x', z)$ [35]. This process, called tomographic reconstruction, was performed on Octopus® [36]. The final 3D rendering and segmentation were performed with Avizo® [37].

The resolution of the reconstructed field, $\mu(x, y, z)$, depends on the resolution of the image field, $P(\varphi, x', z)$; adequate sampling of φ, x', and z is required. After the X-rays pass the sample, they hit a scintillator, which converts the X-rays to visible light before being imaged with a lens onto a scientific CMOS detector. A PCO.edge sCMOS camera (2560 × 2160 pixels) was used with a 2 × lens, giving a 3.3 µm pixel size and a field of view of 8 mm × 2 mm. A total of 1024 images were acquired while the stage was continuously rotating from 0 to 180°.

At beamline 8.3.2 synchrotron radiation provides the photon source, thereby insuring a high flux of photons. The monochromator is tunable over a wide range of photon energy, from 8 to 45 keV allowing for choice of X-ray energy for optimal sample

transmission of 20% through the sample. Because the linear attenuation coefficient, and the resulting transmission through the sample is a function of the energy of the incident X-rays, choosing the appropriate photon energy is important. It is possible to estimate the transmission through the samples tested here from Eq. (1) applied to two components, steel and cement paste, with tabulated linear attenuation coefficients [38]. An ideal sample made of a 0.5-mm-thick piece of steel embedded in 5 mm of cement paste would yield a transmission of 1% at 30 keV, 12% at 40 keV and 30% at 50 keV. After experimentation, a photon energy of 43 keV was found to be optimal. This energy required the exposure time to be about 350 ms for adequate photon counts on the CCD detector with no pixel saturation.

3. Results

3.1. Galvanostatic corrosion

The samples made out of the two different grades of steel were corroded by applying a constant anodic current density of 5 mA cm^{-2} for comparable amounts of time. The potential of the electrode was measured to determine the corrosion stage of the steel reinforcement, and chronopotentiometric curves are presented in Fig. 3. The chosen current density was significantly higher than the 10–100 μA cm^{-2} range that would naturally occur during corrosion of steel in concrete [6,39]; a study by Maaddawy and Soudki [32] showed that current densities above 200 μA cm^{-2} induce unrealistically high strain responses and crack widths. Also, impressing high current probably influenced chemical conditions around the steel, causing acidification around steel surface [31]. Due to the limited availability of the μCT equipment, opting for a higher current density, instead of compromising on the quality of the cement paste, was considered to be a better choice to obtain results in the allocated time frame. Since the aim of the research was to explore the full mechanism of steel corrosion, and to compare the propagation phase of the corrosion of two grades of steel in cement paste (carbon and ferritic stainless steel), the applied current density was considered acceptable.

During the 3 h of galvanostatic corrosion, the two steels showed different behaviours. For the CS specimen, the potential was steady at +1 V versus SCE for the first 45 min, after which it suddenly dropped. It then remained constant at +0.2 V versus SCE before dropping once again after 80 min. At the end, it stabilized at −0.2 V versus SCE. For the FSS sample, the potential stayed at +1.6 V versus SCE for 60 min. After that it slowly decreased and reached its final steady value of +0.25 V versus SCE after 120 min.

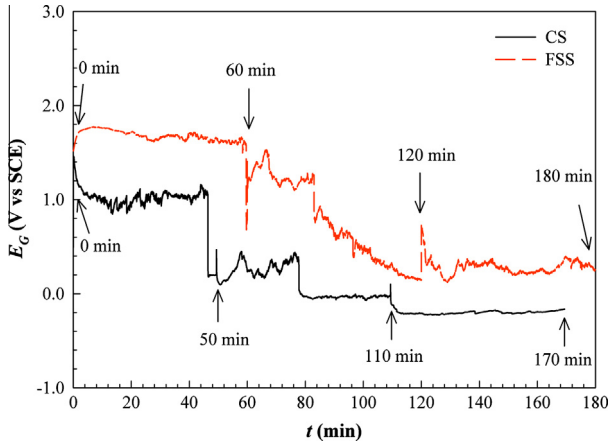


Fig. 3. Chronopotentiometric curves of the carbon steel (CS) and ferritic stainless steel (FSS) samples at an anodic current density of 5 mA cm^{-2}.

3.2. Corrosion products formation and crack patterns in the matrix

The samples were taken out of the solution at three different times and imaged through μCT. Once reconstructed, data were visualized using reconstructed tomograms (Figs. 4 and 5), where at a given height, z_0, the value of the linear attenuation field, $\mu(x, y, z_0)$, is displayed as a greyscale value in a (x, y)-image. Fig. 4 shows the reconstructed tomograms for the CS sample scanned after 0 min, 50 min, 110 min, and 170 min; Fig. 5 shows the reconstructed tomograms for FSS sample after 0 min, 60 min, 120 min, and 180 min. In general for X-rays, the higher the density, the higher is the linear attenuation coefficient. In both figures, steel is denser and is the white circular areas at the centre of the sample. The cement paste is less dense as the grey area all around the reinforcing bar. Within the cement paste the unhydrated cement particles were denser than the cement hydration products; note the lighter shade of grey. Air has zero density and manifests itself as the black areas all around the circular sample, but also in the air voids inside the cement paste. Finally, once active corrosion began, the corrosion products are denser than the cement paste but less dense than steel; they manifested themselves as light grey, similar to the unhydrated cement particles; the former were distinguished from the latter by comparing the images before and after corrosion occurred.

Initially, the reconstructed tomogram of the CS sample showed the round disk of the steel reinforcing bar very close to the centre of the cement paste disk (Fig. 4). Small air voids were present in the cement paste, with few bigger air voids at the bottom left part of the cement paste. After the first 50 min, a thin radial crack formed in the cement paste, which grew larger between 50 and 110 min; at the same time another radial crack formed on the opposite side. At the end of the experiment, cracks 23 μm and 27 μm wide were evidence at the outer-surface of the cement paste. While the steel reinforcing bar in the centre lost some of its cross-sectional area, corrosion products accumulated at the steel/cement paste interface, on the walls of the cracks, and on the wall of the air voids surrounding the steel reinforcing bar. In the enlarged images of Fig. 4, corrosion products propagating from the steel surface could be observed after 110 min, without any visible crack reaching out to the surface. Corrosion products accumulated at the surface of the steel in a homogeneously distributed layer. At the end of the experiment, the corrosion layer had a homogeneous thickness of 40 μm throughout the surface of the steel and was accompanied with homogeneous depletion of the steel content of the reinforcing bar.

Initially, the reconstructed tomograms for the FSS specimen showed that the steel reinforcing bar position was slightly off-centred toward the lower left of the cement paste matrix (Fig. 5). Many air voids smaller than 100 μm were homogeneously distributed in the cement paste. After 60 min, a radial crack had formed in the bottom part of the cement paste and grew larger from 60 to 120 min; at the same time another radial crack formed at a +120° angle (clockwise) from the first one. At the end of the experiment, cracks 27 μm and 74 μm wide were observed on the outer-surface of the cement paste. The corrosion products formed a 73-μm-thick layer only on one side of the steel reinforcing bar in a region delimited by the two radial cracks. In comparison with the CS specimen, the FSS specimen formed a thicker corrosion product layer and cracks were wider on the outer-surface of the cement paste.

3.3. Morphology of the corrosion attack

Steel was the material with the highest linear attenuation coefficient (around 23 cm^{-1} at 43 keV). A binary representation of the steel reinforcing bar was obtained by applying a segmentation threshold, assigning all pixels with a linear attenuation coefficient

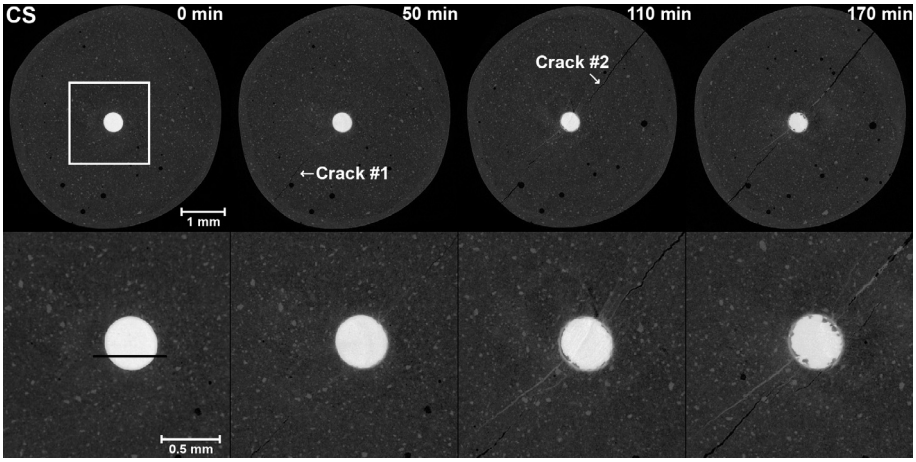


Fig. 4. (Top) Reconstructed tomograms of the carbon steel sample after 0 min, 50 min, 110 min, and 170 min at 5 mA cm^{-2}. (Bottom) Enlarged areas around steel at the same times, as indicated in (Top). The horizontal line across the reinforcement indicates the location of the linear attenuation profiles (Fig. 7).

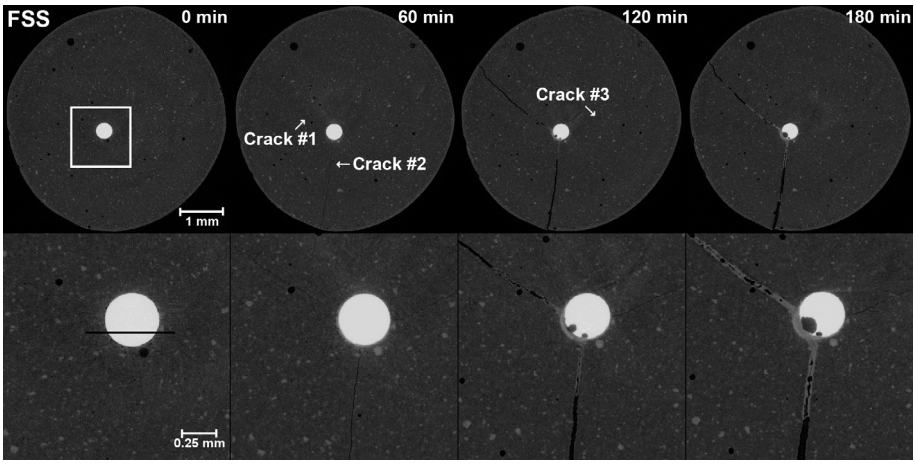


Fig. 5. (Top) Reconstructed tomograms of the FSS specimen after 0 min, 60 min, 120 min, and 180 min at 5 mA cm^{-2}. (Bottom) Enlarged areas around steel at the same times, as indicated in (Top). The horizontal line across the reinforcement indicates the location of the attenuation profiles (Fig. 7).

greater than 15 cm^{-1}. Segmented images of the CS and FSS reinforcing bars are shown on Fig. 6.

From an overall smooth initial surface, the CS specimen showed some homogeneously distributed small pits (Fig. 6a), with sizes at the limit of the resolution of the instrument (pixel size is 3.3 μm), which most likely formed during the thinning of the steel. After impressing an anodic current during the first 50 min, large areas started to corrode away from the surface of the steel. Corrosion propagated gradually from 50 to 110 min, with hollow pits connected in groups and homogeneously distributed around the whole surface of the steel. In the CS specimen, the morphology of the corrosion attack after 170 min had the appearance of general corrosion.

Before galvanostatic corrosion, the surface of the FSS specimen presented a round and smooth surface (Fig. 6b). During the first 60 min, a single pit of significant size (50 μm in diameter) and several smaller pits (diameters of few μm) initiated in the upper part of the sample, making the surface of the steel appear slightly rougher. From 60 to 120 min, the first pit did not grow bigger, but many more pits nucleated and grew. Finally, between 120 and 180 min, several of the pits grew much larger. At the end of the experiment, only a quarter of the surface of the reinforcing bar showed signs of severe corrosion, causing localized loss of steel. In comparison with the CS specimen, pits that formed on the FSS specimen were deeper and mostly disconnected. Some pits were metastable and once formed stopped propagating, while other pits interconnected and propagated deeper.

3.4. Type of corrosion products

Attenuation length profiles at the steel/cement paste interface were obtained in order to evaluate the dynamic of the formation of corrosion products (Fig. 7).

The linear attenuation coefficient is high for the middle steel portion of the sample, and dropped sharply on the sides at the interface with the cement paste. For the CS specimen (Fig. 7a), the linear attenuation coefficient of carbon steel was measured to be 19.7 cm^{-1}, and the cement paste 1.7 cm^{-1}. Later, steel was consumed and the width of the steel portion was reduced, while corrosion products accumulated at the interface with linear attenuation coefficients of 5–10 cm^{-1}.

The initial attenuation profile for the FSS specimen showed similar behaviour compared to the CS specimen (Fig. 7b). The linear attenuation coefficient of the FSS specimen was measured to be 18.9 cm^{-1}, and the cement paste 1.6 cm^{-1}. After 60 min, some corrosion products formed at the interface, increasing its linear attenuation coefficient. At 120 and 180 min, a corrosion pit formed and a larger portion of the steel was etched away, while corrosion

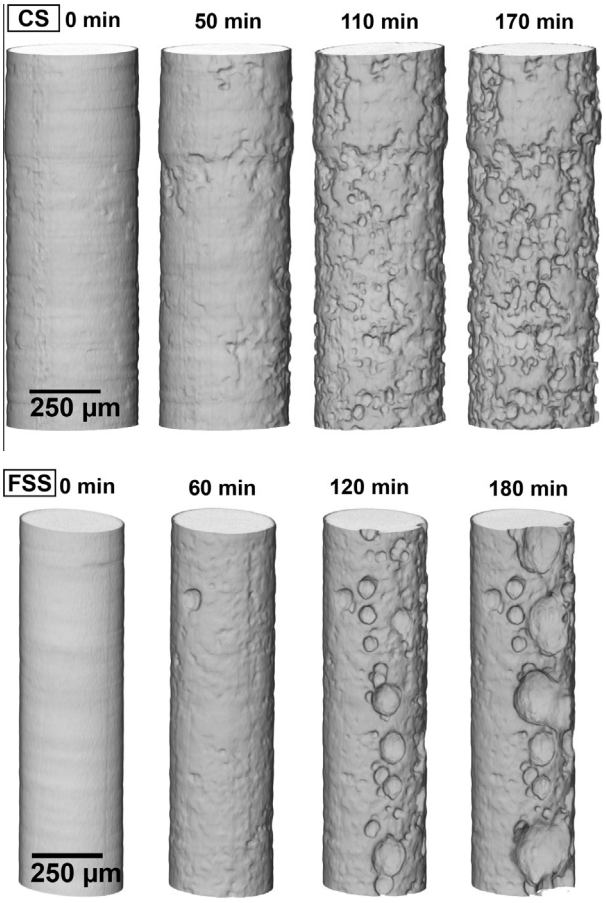


Fig. 6. Binary segmentation showing the surface of the carbon steel (CS), and the ferritic stainless steel (FSS) samples at the different times.

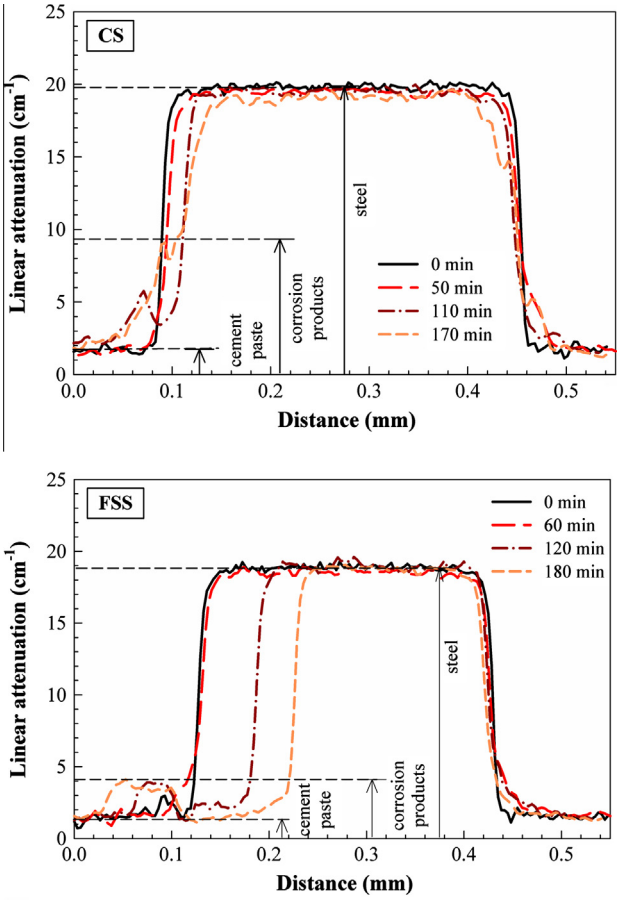


Fig. 7. Linear attenuation profiles across the interfaces steel/cement paste after 0 min, 50 min, 110 min, and 170 min for the carbon steel sample (CS), and after 0 min, 60 min, 120 min, and 180 min for the ferritic stainless steel sample (FSS). See Figs. 4 and 5 to locate the profile lines on the samples.

products accumulated on the outside of the cavity left by the steel. These corrosion products had an average linear attenuation coefficient of 3.6 cm^{-1}.

4. Discussion

4.1. Corrosion mechanism

When steel is exposed to alkaline environment, such as the one found in ordinary Portland cement concrete, a passive film naturally forms. Initially, this passive film protects the steel from corroding. Fluctuations of the potential during constant current are indications of the changes of the passive layer on the surface of the steel. In a typical galvanostatic polarisation experiment conducted in a pit promoting electrolyte, such as sodium chloride solution, the resulting chronopotentiometric curve will have distinct phases related to different surface phenomena: a first sharp increase in potential indicates pit nucleation, then pit growth is decreasing the potential with time, and eventually a stationary potential value is reached, indicating pit repassivation [40]. At the beginning of exposure to high current density, for both steels, fluctuations of the potential were visible, with potential suddenly increasing and soon afterwards decreasing to a constant value. These fluctuations were more pronounced in the case of CS, possibly indicating more corrosion nucleation sites.

For the CS sample, the potential suddenly dropped down of about 1 V after 45 min, while for the FSS sample, the potential slowly decreased after 1 h of galvanostatic corrosion (Fig. 3). The decay of potential was caused by a decrease of the specific electrical resistance, with several hypotheses to explain its decrease. One hypothesis is the ingress of chlorides in the cement matrix, directly influencing the conductivity of the matrix, and therefore decreasing its resistivity. However, the migration of chlorides would not cause such a sudden decay in potential. Next, the total resistance can decrease by the initiation of corrosion, and the formation of products on the steel surface [33]. Furthermore, as the pits grew, their areas increased, so the average current density would decrease. Since the current density was kept constant, the potential decreased to support the lower current density [40]. Finally, a sudden decay in potential could also be attributed to the formation of cracks, which were quickly filled with the conductive testing solution [41]. This latter hypothesis was supported by the radial cracks shown in Figs. 4 and 5, the formation of these cracks could also be observed as a reason for a sudden potential decay evident in Fig. 3.

The whole surface of the CS sample homogeneously corroded away, and at the end of the experiment the corrosion attack on the carbon steel appeared generalized (Fig. 6a). It seemed that the whole bar started to corrode at the same time, and when the passive film broke down, even at a small location, a microcell formed, and the rest of the bar depassivated as well. In the case of the FSS specimen, the potential slightly dropped after 60 min, just before being imaged. The µCT scan revealed the presence of a single pit (Fig. 6b). Upon continuation of the galvanostatic polarisation, the potential increased to a level slightly lower than before the decrease. This was the initiation step of the pitting attack of stainless steel, at the earlier stages of pit propagation when the pits

are still very small, they can repassivate spontaneously. This is called a metastable pit growth; pits form but are passivated again just after nucleation [42]. When a small area of the film depassivated, the rest of the passive film remained strong enough to hold and not corrode, and no metastable pits transformed into stable pit propagation [20]. The last step in this process is the stable pit propagation, which is reached when spontaneous repassivation is no longer possible. When pits on the FSS sample eventually transformed into stable pits, small areas corroded away. However small these areas were, the steel cross section was significantly reduced. At the end of experiment only a quarter of the surface of the FSS sample was attacked by corrosion (Fig. 6b), confirming the localized aspect of the corrosion of the FSS bar.

The potential over time remained higher for the FSS sample compared to the CS sample. Frangini et al. [40] measured that higher values of pitting potentials were indications of the formation of a more protective passive film on stainless steels. The values of potential for both steel types were higher than that usually obtained by potentiodynamic polarisation of steel in alkaline environment contaminated with chlorides; for example results in [11,13,15]. It is usual that galvanostatic measurements give more noble potentials at which passive films breaks down, since the maximum obtained potential reflects the sum of two competing processes: passivation and pit nucleation. Furthermore, the value of the potential is highly dependent on the applied current, and with higher anodic current, pit nucleation occurs at higher potentials [40].

The volume of corroded steel was measured from the segmented images of the two steels using the quantification tools in the software Avizo®. It was then divided by the sample length to give its average cross-sectional area, A; the measured average penetration depth, δ_m, was computed by dividing the area by the perimeter of the initial cross-section with radius, r_0:

$$\delta_m = \frac{A_0 - A}{2\pi r_0} \tag{4}$$

From the reconstructed tomograms, the depth of the deepest pits was also measured and compared to the average loss of steel measured from μCT (Table 2). For the CS sample, the deepest pit grew from 8 μm at to 83 μm by the end of experiment. Note that the pit at the beginning of the experiment is most likely not a corrosion pit, but a machining flaw. At the end of the galvanostatically-controlled corrosion, the deepest pit was almost 6 times deeper than the average general penetration depth. This value is in the range of values from other studies, where the maximum penetration was measured to be 4–8 times the average general penetration [43]. For the FSS specimen, the deepest pit grew to be 124-μm-deep by the end of experiment. It was about 12 times greater than the average general penetration depth. Therefore, in the case of FSS specimen when the pits eventually transformed into stable pits, small areas were corroded away, with consequent important local cross-section reduction. The corrosion on the FSS specimen was localized, as opposed to the generalized corrosion seen on the CS specimen.

Table 2
Thickness loss measured by μCT during galvanostatic corrosion at an anodic current of 5 mA cm^{-2}.

Thickness loss (μm)	0 min	50 min	110 min	170 min
CS				
Average	0	3.5	8.0	13.9
Deepest pit	8	18	46	83
	0 min	60 min	120 min	180 min
FSS				
Average	0	1.8	5.7	10.9
Deepest pit	0	41	85	124

Faraday's law of electrolysis provides a convenient way to predict the amounts of species that are produced/reacted during an electrochemical reaction, e.g., for $A \rightarrow A^{n+} + n.e^-$:

$$m = \frac{ItM}{nF} \tag{5}$$

where m is the mass of steel consumed, I is the current, t is the time, M is the atomic weight of the metal, n is the ionic charge, and F is the Faraday's constant. The computed average penetration depth, δ_c, is calculated by dividing m by the exposed surface of metal, and by its density, ρ:

$$\delta_c = \frac{itM}{nF\rho} \tag{6}$$

where $i = \frac{I}{A}$ is the current density. For iron, $n = 2$, $M = 55.9$ g mol^{-1}, $\rho = 7.87$ g cm^{-3}, hence:

$$\delta_c = 1.332it\,(\mu m) \tag{7}$$

with i in mA cm^{-2} and t in hours. This calculated penetration depth, δ_c, is compared with the measured values, δ_m (Fig. 8).

The penetration depth predicted by the Faraday's law was, in both cases, larger than the volume loss measured by the μCT experiments. At the beginning of the galvanostatic corrosion, current was used and metastable pits were formed: the steel was still in a passive state, and active corrosion had not formed yet. After the initiation period, once the passive film broke down, the average penetration grew linearly with time, at a rate close to the rate predicted by Faraday. Similar results were found by Andrade et al., while measuring the weight loss by gravimetric method [44]. Some corrosion mechanism models include nonlinear corrosion products growth. After corrosion products have formed, they influence the behaviour of the steel; a layer of corrosion products blocks the continuous formation of new products [4]. The effect of the accumulation of corrosion products on the corrosion product growth is described by nonlinear equations [3]; however, no evidence of this behaviour was observed in this experiment, most probably due to the high galvanostatic current density. The observed propagation of corrosion product was important and might have arisen from this high electrical field.

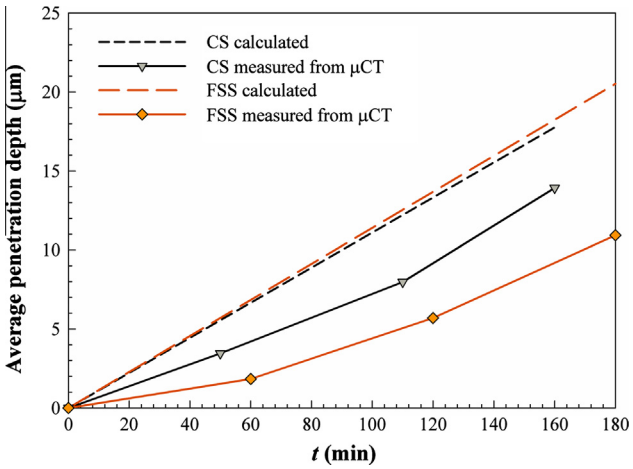


Fig. 8. Comparison between the steel average corrosion penetration depth predicted by Faraday's law (δ_c) and measured by μCT (δ_m) for the carbon and the ferritic stainless steel.

4.2. Crack formation and propagation of corrosion products

At the same time the passive film broke down, radial cracks initiated on both steels (Figs. 4 and 5). Corrosion products accumulated at the interface between steel and cement paste, and their expansion generated a tensile hoop stress in the cement paste matrix. When the pressure reached the tensile strength of the matrix, the cement paste broke, and radial cracks propagated from the steel toward the exterior of the sample. Knowing the linear attenuation coefficient of the phases present in the samples, the tomography data was segmented to obtain a 3D image of the system corrosion products/crack. The voxels with linear attenuation coefficients from 0 to 1 cm^{-1} were assigned to voids and cracks, from 2.2 to 9 cm^{-1} to corrosion products, and above 9 cm^{-1} to steel. The 3D structure of the samples was visualized by showing the cracks in shades of black and the corrosion products in shades of orange (Fig. 9). Sharp contrasts were obtained between empty cracks (black voxels) and the cement paste (shades of grey), therefore the sensitivity of crack detection was close to the technique's spatial resolution, which is twice the voxel size, i.e. 6.6 μm.

Initially, the CS specimen did not show any trace of corrosion products or cracks. After 50 min, corrosion products had accumulated around the steel reinforcing bar. They also started to propagate outward, filling up the walls of a 0.3-mm-diameter air void. Two thin radial cracks formed: crack #1 reached the external face of the cement paste, while crack #2 was still small. Between 50 and 110 min, more corrosion products accumulated around the steel bar, and some propagated out and were located next to crack #1, but did not follow it. Crack #2 grew longer and reached the external face of the cement paste matrix. Between 110 and 170 min, more corrosion products accumulated around the steel bar, and continued to propagate next to crack #1. Other corrosion products started to propagate and deposit along crack #2.

Initially, the FSS specimen did not show any trace of corrosion products or cracks. After 60 min, corrosion products had accumulated around the steel reinforcing bar and filled out two small air voids next to the reinforcing bar. Three radial cracks formed at 120° angles from each other: crack #1 reached the external face of the cement paste, while crack #2 was small, and crack #3 even smaller. Between 60 and 120 min, crack #1 and crack #2 grew larger, and more corrosion products accumulated around the steel bar and propagated out into crack #1 and crack #2, depositing on their walls. Crack #3 remained stable and no corrosion products propagated into it. Between 120 and 180 min, more corrosion products formed. They propagated in a non-uniform front into the cracks. The reinforcing bar of the FSS sample was off-centred, causing different cover thicknesses at different sides; it was the smallest on the lower-left side (Fig. 5). Under the same electrochemical conditions, the corrosion of steel at this side became easier than at other sides, major corrosion happened, and it led to the two main cracks. On the other FSS sample with an off-centred reinforcing bar, the same behaviour was observed, with the bar corroding locally on the side with smallest cover thickness.

One model for crack formation and propagation of corrosion products is the following [3,21]: (1) the crack initiates and grows radially outward; (2) once it has fully cracked the concrete cover, the outer solution can directly reach the steel/cement paste interface and corrosion forms at the mouth of the crack; and (3) the accumulation of corrosion products at the tip of the mouth causes stresses that open the crack linearly with the distance to the centre. A corollary to this three-step mechanism is that corrosion products can only propagate through an open crack. For the FSS specimen in the reconstructed tomograms of Fig. 5, no clear corrosion products propagated out of the crack that did not reach the surface of the cement paste cover (crack #3). Furthermore, on the CS specimen in Fig. 4, it appeared that corrosion products propagated out of a crack that did not reach the concrete cover. Subsequent analysis of a bigger dataset with longer surfaces (not shown here) demonstrated that the crack actually belonged to a crack network that contained an open crack. This was in agreement with the aforementioned three-step mechanism described.

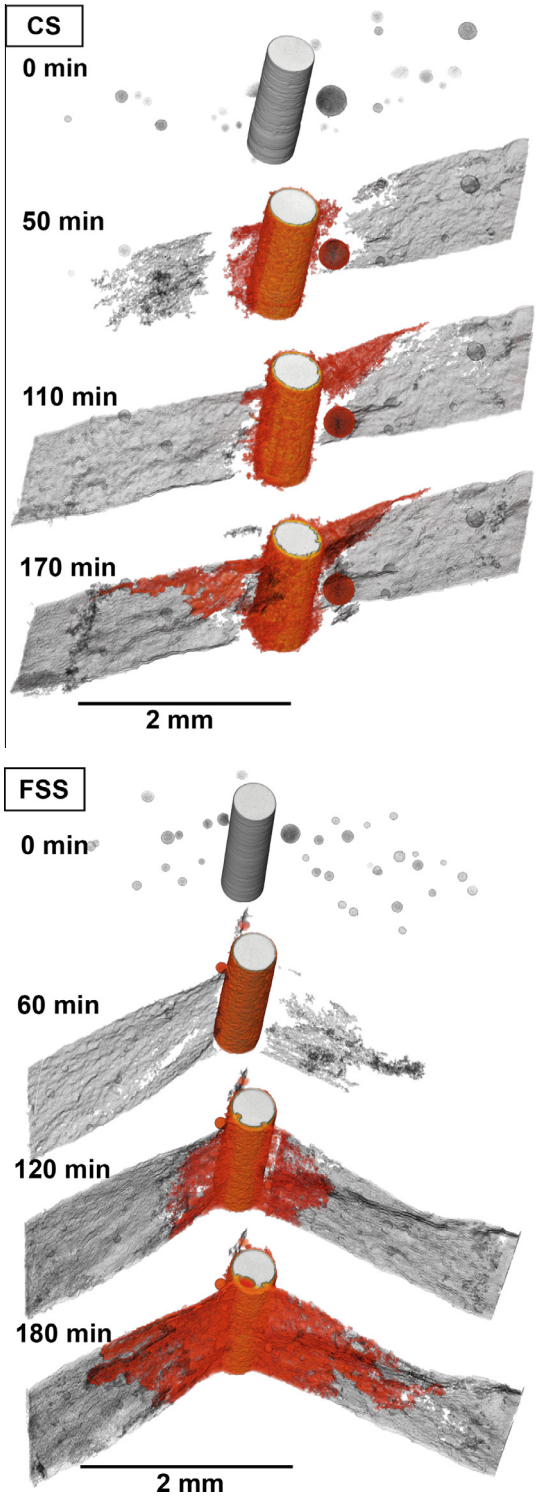


Fig. 9. 2-phase segmentation of the carbon steel (CS) and the ferritic stainless steel (FSS) samples at different times. The steel is in light grey, the propagating corrosion products are in orange, and the propagating cracks and the air voids are in dark grey. (For interpretation of the references to colour in this figure legend, the reader is referred to the web version of this article.)

Information about the type of corrosion products could be deducted by comparing the experimental linear attenuation coefficient with its computed value, μ:

$$\mu = \rho \sum f_i \mu_i \quad (8)$$

where the material has a density, ρ [2], and each atomic element, i, has an atomic weight fraction, f_i, and a mass attenuation coefficients, μ_i [38]. At photon energy 43 keV, the computed linear attenuation coefficient of steel is 23 cm^{-1}, and the cement paste 1.7 cm^{-1}. For corrosion products, it was 13 cm^{-1} for denser iron oxides, like iron(II)-oxide FeO, and it was 6.6 cm^{-1} (resp. 5.7 cm^{-1}) for less dense iron oxides, like iron hydroxides $Fe(OH)_2$ (resp. $Fe(OH)_3$). For hydrated iron hydroxide $Fe(OH)_3{\cdot}3H_2O$, the linear attenuation was even lower, 4.2 cm^{-1}.

At the steel interface of the CS specimen, linear attenuation coefficients covered a wide range from 5 to 10 cm^{-1} (Fig. 7a). These values are below the values for iron(II)-oxide but are in the range of the iron hydroxides. At the wall of the pit cavity on the FSS specimen, the average linear attenuation coefficient was 3.6 cm^{-1} (Fig. 7b). This value was close to the linear attenuation coefficient of hydrated iron hydroxide. Hydrated iron hydroxides are less often found as corrosion products during "destructive" observations of corroded samples [5,45], due to the fact that the products are inevitably exposed to air during preparation of samples for investigation. Because the values of linear attenuation coefficient were different between the both steels, this might indicate that the types of corrosion products forming in both cases were different. However, determination of exact composition of the corrosion products is not obvious. First, the voxel size of the μCT instrument was 3.3 μm × 3.3 μm × 3.3 μm so it was not possible to distinguish microstructural features that were smaller than this size. In particular, corrosion products can form a porous network with pores below the micrometre scale; this may lower the apparent density and attenuation coefficient. Second, the predicted values of the linear attenuation coefficients are computed from tabulated values of the density of the products that can lead to large uncertainties. For a more precise determination of the type of corrosion products, spectroscopy work would be more appropriate, enabling distinctions between oxidation states.

5. Conclusion

This work provided qualitative as well as quantitative information about the propagation of corrosion of steel embedded in cement paste. Applying an external anodic current of 5 mA cm^{-2} accelerated the corrosion rate in a reproducible manner on two different specimens, one containing carbon steel, and the other ferritic stainless steel. The crack patterns and the propagation of the corrosion products were measured non-invasively by μCT, allowing the analysis of the mechanisms in real time. The experimental image sets resolved the cracked cement paste, the propagating corrosion products, and the corroded steel with a resolution of few micrometres. Quantitative measurements of the linear attenuation coefficients and the size of the features were also performed.

Five major conclusions can be drawn from this work:

(1) X-ray microtomography can be used for 3D *in situ*, non-destructive monitoring of the full mechanism of steel corrosion in cement paste. After a passivity period where no sign of corrosion was seen, the surface of the steel reinforcement was progressively etched away, and the corrosion products accumulated at the steel/concrete interface. When they reached a certain pressure, the cement paste fractured, and cracks propagated in the concrete matrix. The corrosion products then propagated outward along the cracks, eventually depositing on the walls of the cracks.

(2) With respect to the morphology, carbon steel showed a homogeneous corrosion, with the entire surface gradually etched away. Conversely, ferritic stainless steel corroded locally, with the formation of corrosion pits distributing over a quarter of its surface. The deepest pit in the case of carbon steel was about 6 times greater than the average general penetration depth, and in the case of ferritic stainless steel, 12 times greater.

(3) After depassivation of steel, the average rate of steel loss measured by μCT correlated well with the rate predicted by Faraday's law of electrolysis.

(4) Localised corrosion attack observed on ferritic stainless steel specimen led to concentrations of stresses that caused wider cracks in the cement paste compared to the generalized corrosion of carbon steel.

(5) Corrosion was induced by strong levels of current flow, and corrosion products were attracted away from the steel surface by strong electrical migration. This prevented their further accumulation at the steel surface.

Acknowledgements

This publication was based on work supported by Award No. KUS-I1-004021, made by King Abdullah University of Science and Technology (KAUST). This research was supported in part by Unity through Knowledge Fund (UKF), Croatian Ministry of Science, Education and Sport (Grant No. 73/10). The Advanced Light Source is supported by the Director, Office of Science, Office of Basic Energy Sciences, of the U.S. Department of Energy under Contract No. DE-AC02-05CH11231.

References

[1] K. Tuutti, Corrosion of Steel in Concrete, in: Tech. Report, Swedish Cement and Concrete Research Institute, Stockholm, 1982.
[2] P. Patnaik, Handbook of Inorganic Chemicals, McGraw-Hill, 2003.
[3] Y. Liu, R.E. Weyers, Modeling the time-to-corrosion cracking in chloride contaminated reinforced concrete structures, ACI Mater. J. 95 (1998) 675–681.
[4] K. Bhargava, A.K. Ghosh, Y. Mori, S. Ramanujam, Modeling of time to corrosion-induced cover cracking in reinforced concrete structures, Cem. Concr. Res. 35 (2005) 2203–2218.
[5] S. Caré, Q.T. Nguyen, V. L'Hostis, Y. Berthaud, Mechanical properties of the rust layer induced by impressed current method in reinforced mortar, Cem. Concr. Res. 38 (2008) 1079–1091.
[6] C. Andrade, C. Alonso, F.J. Molina, Cover cracking as a function of bar corrosion: Part I-Experimental test, Mater. Struct. 26 (1993) 453–464.
[7] T. Liu, R.E. Weyers, Modeling the dynamic corrosion process in chloride contaminated concrete structures, Cem. Concr. Res. 28 (1998) 365–379.
[8] C. Lu, W. Jin, R. Liu, Reinforcement corrosion-induced cover cracking and its time prediction for reinforced concrete structures, Corros. Sci. 53 (2011) 1337–1347.
[9] Y. Zhao, H. Dai, W. Jin, A study of the elastic moduli of corrosion products using nano-indentation techniques, Corros. Sci. 65 (2012) 163–168.
[10] Y. Zhao, B. Hu, J. Yu, W. Jin, Non-uniform distribution of rust layer around steel bar in concrete, Corros. Sci. 53 (2011) 4300–4308.
[11] S.M. Alvarez, A. Bautista, F. Velasco, Corrosion behaviour of corrugated lean duplex stainless steels in simulated concrete pore solutions, Corros. Sci. 53 (2011) 1748–1755.
[12] C.M. Abreu, M.J. Cristóbal, R. Losada, X.R. Nóvoa, G. Pena, M.C. Pérez, Comparative study of passive films of different stainless steels developed on alkaline medium, Electrochim. Acta 49 (2004) 3049–3056.
[13] H. Luo, C.F. Dong, X.G. Li, K. Xiao, The electrochemical behaviour of 2205 duplex stainless steel in alkaline solutions with different pH in the presence of chloride, Electrochim. Acta 64 (2012) 211–220.
[14] B.G. Callaghan, The performance of a 12% chromium steel in concrete in severe marine environments, Corros. Sci. 35 (1993) 1535–1541.
[15] A. Pardo, M.C. Merino, A.E. Coy, F. Viejo, R. Arrabal, E. Matykina, Pitting corrosion behaviour of austenitic stainless steels – combining effects of Mn and Mo additions, Corros. Sci. 50 (2008) 1796–1806.
[16] L. Babout, T.J. Marrow, D. Engelberg, P.J. Withers, X-ray microtomographic observation of intergranular stress corrosion cracking in sensitised austenitic stainless steel, Mater. Sci. Tech. Ser. 22 (2006) 1068–1075.
[17] D.A. Horner, B.J. Connolly, S. Zhou, L. Crocker, A. Turnbull, Novel images of the evolution of stress corrosion cracks from corrosion pits, Corros. Sci. 53 (2011) 3466–3485.

[18] S.M. Ghahari, A.J. Davenport, T. Rayment, T. Suter, J. Tinnes, C. Padovani, J.A. Hammons, M. Stampanoni, F. Marone, R. Mokso, In situ synchrotron X-ray micro-tomography study of pitting corrosion in stainless steel, Corros. Sci. 53 (2011) 2684–2687.
[19] Y. Tsutsumi, A. Nishikata, T. Tsuru, Pitting corrosion mechanism of Type 304 stainless steel under a droplet of chloride solutions, Corros. Sci. 49 (2007) 1394–1407.
[20] R.D. Moser, P.M. Singh, L.F. Kahn, K.E. Kurtis, Chloride-induced corrosion resistance of high-strength stainless steels in simulated alkaline and carbonated concrete pore solutions, Corros. Sci. 57 (2012) 241–253.
[21] Y. Zhao, J. Yu, B. Hu, W. Jin, Crack shape and rust distribution in corrosion-induced cracking concrete, Corros. Sci. 55 (2012) 385–393.
[22] K.L. Scrivener, Backscattered electron imaging of cementitious microstructures: understanding and quantification, Cem. Concr. Compos. 26 (2004) 935–945.
[23] A. Michel, B.J. Pease, M. Geiker, H. Stang, J.F. Olesen, Monitoring reinforcement corrosion and corrosion-induced cracking using non-destructive X-ray attenuation measurements, Cem. Concr. Res. 41 (2011) 1085–1094.
[24] E. Gallucci, K. Scrivener, A. Groso, M. Stampanoni, G. Margaritondo, 3D experimental investigation of the microstructure of cement pastes using synchrotron X-ray microtomography (μCT), Cem. Concr. Res. 37 (2007) 360–368.
[25] T. Marrow, L. Babout, A. Jivkov, P. Wood, D. Engelberg, N. Stevens, P.J. Withers, R.C. Newman, Three dimensional observations and modelling of intergranular stress corrosion cracking in austenitic stainless steel, J. Nucl. Mater. 352 (2006) 62–74.
[26] A. Česen, T. Kosec, A. Legat, Characterization of steel corrosion in mortar by various electrochemical and physical techniques, Corros. Sci. 75 (2013) 47–57.
[27] T. Tian, K. Chen, A.A. Macdowell, D. Parkinson, Y. Lai, K.N. Tu, Quantitative X-ray microtomography study of 3-D void growth induced by electromigration in eutectic SnPb flip-chip solder joints, Scripta Mater. 65 (2011) 646–649.
[28] J.B. LeBret, M.G. Norton, D.F. Bahr, Examination of crystal defects with high-kV X-ray computed tomography, Mater. Lett. 59 (2005) 1113–1116.
[29] P.H. Baker, D. Bailly, M. Campbell, G.H. Galbraith, R.C. McLean, N. Poffa, C.H. Sanders, The application of X-ray absorption to building moisture transport studies, Measurement 40 (2007) 951–959.
[30] P.J.M. Monteiro, A.P. Kirchheim, R.S. Chae, P. Fischer, A.A. MacDowell, E. Schaible, H.R. Wenk, Characterizing the nano and microstructure of concrete to improve its durability, Cem. Concr. Compos. 31 (2009) 577–584.
[31] A. Poursaee, C.M. Hansson, Potential pitfalls in assessing chloride-induced corrosion of steel in concrete, Cem. Concr. Res. 39 (2009) 391–400.
[32] T.A. El Maaddawy, K.A. Soudki, Effectiveness of impressed current technique to simulate corrosion of steel reinforcement in concrete, J. Mater. Civ. Eng. 15 (2003) 41–47.
[33] S. Caré, A. Raharinaivo, Influence of impressed current on the initiation of damage in reinforced mortar due to corrosion of embedded steel, Cem. Concr. Res. 37 (2007) 1598–1612.
[34] A.A. MacDowell, D.Y. Parkinson, A. Haboub, E. Schaible, J.R. Nasiatka, C.A. Yee, J.R. Jameson, J.B. Ajo-Franklin, C.R. Broderson, A.J. McElrone, X-ray Micro-Tomography at the Advanced Light Source, in: Proceedings of SPIE 8506, vol. 18, 2012.
[35] A.C. Kak, M. Slaney, Principles of Computerized Tomographic Imaging, IEEE Press, New York, 1999.
[36] J. Vlassenbroeck, B. Masschaele, V. Cnudde, M. Dierick, K. Pieters, L. Van Hoorebeke, P. Jacobs, Octopus 8: A High Performance Tomographic Reconstruction Package for X-ray Tube and Synchrotron micro-CT, in: Advances in X-ray Tomography for Geomaterials, ISTE, 2010, pp. 167–173.
[37] http://www.vsg3d.com/avizo/ (accessed on Jan25.01.14).
[38] J.H. Hubbell, S.M. Seltzer, Tables of X-ray Mass Attenuation Coefficients and Mass Energy-Absorption Coefficients, National Institute of Standards and Technology, Physical Reference Data, 5632, 1996.
[39] C. Christodoulou, C.I. Goodier, S.A. Austin, J. Webb, G. Glass, On-site transient analysis for the corrosion assessment of reinforced concrete, Corros. Sci. 62 (2012) 176–183.
[40] S. Frangini, N. De Cristofaro, Analysis of the galvanostatic polarization method for determining reliable pitting potentials on stainless steels in crevice-free conditions, Corros. Sci. 45 (2003) 2769–2786.
[41] C. Fang, K. Lundgren, L. Cheng, C. Zhu, Corrosion influence on bond in reinforced concrete, Cem. Concr. Res. 34 (2004) 2159–2167.
[42] Y. Zuo, H. Wang, J. Xiong, The aspect ratio of surface grooves and metastable pitting of stainless steel, Corros. Sci. 44 (2002) 25–35.
[43] J.A. González, C. Andrade, C. Alonso, S. Feliu, Comparison of rates of general corrosion and maximum penetration on concrete embedded steel reinforcement, Cem. Concr. Res. 25 (1995) 257–264.
[44] C. Andrade, J.A. González, Quantitative measurements of corrosion rate of reinforcing steels embedded in concrete using polarization resistance measurements, Mater. Corros. 29 (1978) 515–519.
[45] D.A. Koleva, J. Hu, A.L.A. Fraaij, P. Stroeven, N. Boshkov, J.H.W. de Dewit, Quantitative characterisation of steel/cement paste interface microstructure and corrosion phenomena in mortars suffering from chloride attack, Corros. Sci. 48 (2006) 4001–4019.